

Robust operation of a GaAs tunable barrier electron pump

S. P. Giblin,¹ M. -H. Bae,² N. Kim,² Ye-Hwan Ahn,^{2,3} and M. Kataoka¹

¹*National Physical Laboratory, Hampton Road, Teddington, Middlesex TW11 0LW, United Kingdom*

²*Korea Research Institute of Standards and Science, Daejeon 34113, Republic of Korea*

³*Department of Physics, Korea University, Seoul 02841, Republic of Korea*

(Dated: 2 October 2018)

We demonstrate the robust operation of a gallium arsenide tunable-barrier single-electron pump operating with 1 part-per-million accuracy at a temperature of 1.3 K and a pumping frequency of 500 MHz. The accuracy of current quantisation is investigated as a function of multiple control parameters, and robust plateaus are seen as a function of three control gate voltages and RF drive power. The electron capture is found to be in the decay-cascade, rather than the thermally-broadened regime. The observation of robust plateaus at an elevated temperature which does not require expensive refrigeration is an important step towards validating tunable-barrier pumps as practical current standards.

PACS numbers: 1234

I. INTRODUCTION

The controlled transport of single electrons in mesoscopic devices has attracted much attention as a conceptually simple primary standard of electric current¹. Very precise control of electrons has been achieved using chains of mesoscopic normal metal islands², but limited to slow pumping rates $\lesssim 10$ MHz due to the fixed RC time-constant of the junctions between the islands. At the present time, the most practically useful combination of accuracy and high electron pumping rate has been achieved using electrostatically gated semiconductor quantum dots (QDs) operated as non-adiabatic tunable-barrier pumps³ in the low-temperature decay cascade regime⁴. Using state-of-the-art current measurement techniques^{5,6}, there have been several reports of pumped current accurate at the part-per-million (ppm) level or better, at pump repetition rates in the range $0.5 \text{ GHz} \leq f \leq 1 \text{ GHz}$, generating current $80 \text{ pA} \leq I_P = ef \leq 160 \text{ pA}$ ^{5,7-11}, where e is the elementary charge. These studies were performed on a variety of device architectures: etch-defined^{5,8,10} and gate-defined⁷ QDs in GaAs heterostructures, and silicon nano-wire MOSFETs⁹. While very promising for the metrological application of electron pumps, most of these studies were performed on carefully tuned devices. The required robustness of the current against changes in the pump control parameters has only recently begun to be investigated with high precision^{11,12}, and only in one type of etch-defined pump.

In this study, we broaden the study of robustness, and investigate the gate-defined tunable barrier pump^{7,13}. Most significantly for the application of pumps as practical current standards, we perform our measurements at ~ 1.3 K, the temperature of pumped helium-4. This is in contrast to previous robustness studies^{11,12,14} which were carried out at dilution refrigerator temperatures. Using a rigorous statistical approach to evaluate the plateau extension and flatness, we find robust plateaus in all

the tuning parameters we investigated, flat to within the $\sim 2 \times 10^{-6}$ relative statistical uncertainty of each data point. Long measurements with the device in an optimally-tuned condition gave a current equal to ef within a relative total uncertainty of 8.6×10^{-7} . We also show that despite the elevated temperature, the pump was operating in the decay-cascade regime and not the thermally-broadened regime predicted¹⁵ and observed¹⁶ at higher temperatures. Furthermore, the device was affected by a significant amount of charge noise. The robust performance of the pump under these non-ideal conditions is encouraging evidence that the semiconductor electron pump can fulfill a role as a practical current standard.

This paper is structured as follows: Section II describes the characterization and measurement technique. Section III presents the main experimental results in which we show that the pump current displays flat plateaus over a wide range of several tuning parameters. In section IV we analyze the statistical fluctuations of the current on the plateaus, and show that there is no indication of structure on the plateaus within the measurement uncertainty. Finally in section V we show that the pump is operating in the decay-cascade regime, and not in the thermal-equilibrium regime, even at the elevated temperature.

II. CHARACTERISATION

The pump used in this study (see SEM image in Fig. 1a) was realised in a 2-dimensional electron gas (2-DEG) in a GaAs-AlGaAs heterostructure with metallic surface gates. The sample was fabricated using techniques described previously^{7,13}, and measured at a temperature of ~ 1.3 K. DC voltages $V_{G1} - V_{G6}$ defined a quantum dot in the region between the gates, and a sinusoidal AC voltage at $f = 500$ MHz was added to gate 1 using a room-temperature bias-T, to pump electrons

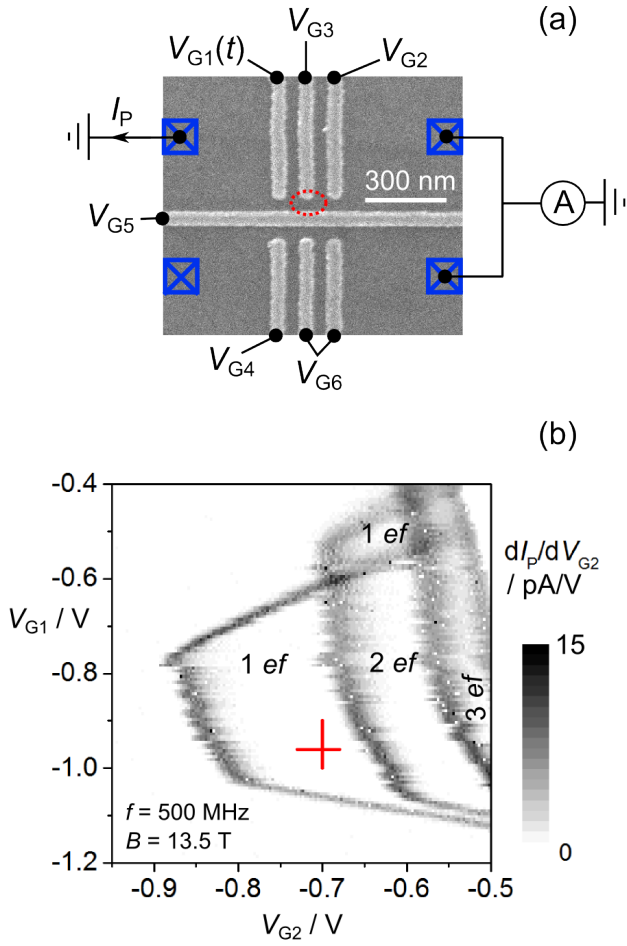


FIG. 1. (a): Scanning electron microscope image of a device from the same fabrication batch as the one used in this study. Crossed boxes indicate ohmic contacts. Metallic gates show up as light grey. The connection of the 6 control voltages to the gates is indicated, and when the gates are energized the QD forms in the approximate location indicated by the red dashed oval. An AC voltage added to gate 1 pumps electrons from left to right, generating a current I_P with conventional sign flowing from right to left. (b): Derivative map of pumped current at $f = 500$ MHz, $B = 13.5$ T and $P_{RF} = 5.2$ dBm as a function of V_{G1} and V_{G2} . The current on the quantised plateaus (white regions of the plot) is indicated in multiples of ef . The red lines indicate the ranges of the high-accuracy scans shown in Figs. 2a,b,e,f.

from the source to the drain. The AC source had an output power P_{RF} , calibrated for a 50Ω load, and the total attenuation of the 50Ω co-axial line between the source and the device was ≈ 4 dB. A magnetic field $B = 13.5$ T was applied perpendicular to the plane of the sample^{17–19}. The pump current I_P was measured in two modes; normal-accuracy and high-accuracy. In normal-accuracy mode, used for rapid characterization, the current was amplified by a room-temperature transimpedance amplifier, with an uncertainty in the gain calibration of $\sim 2 \times 10^{-4}$. For high-accuracy measure-

ments, I_P was compared with a reference current derived from applying a voltage across a calibrated $1 \text{ G}\Omega$ standard resistor.^{5,7,9} In this mode the amplifier measures the small difference between the pump and reference currents, and provided this difference is made less than 0.05% of I_P , by tuning the reference current, the calibration uncertainty of the amplifier contributes less than 1×10^{-7} to the total relative uncertainty. We are chiefly interested in the deviation of I_P from its expected quantised value ef , so we define the dimensionless normalised deviation, $\Delta I_P \equiv (I_P - ef)/ef$. Likewise, all uncertainties in ΔI_P will be expressed as relative uncertainties in dimensionless units. The RF modulation of the entrance gate, and the reference current source are turned on and off synchronously with a cycle time of 40 seconds to eliminate instrumental offsets. The on-off cycle is repeated n_{cyc} times. To reject linear drift in the offset current, our data analysis routine calculates ΔI_P using the data from the 'off' part of the cycle and half of the data from the two adjacent 'on' parts, thus generating $n_{cyc} - 1$ statistically independent values of ΔI_P with standard deviation σ_1 ²⁰. These values are then averaged to yield a mean ΔI_P with statistical uncertainty $U_{ST} = \sigma_1/\sqrt{n_{cyc} - 1}$ (all uncertainties reported in this paper are 1 sigma standard uncertainties). The relative systematic uncertainty in ΔI_P is dominated by the calibration uncertainty of the standard resistor, $U_{1G} = 8 \times 10^{-7}$, with an additional small contribution due to the voltage measurement $U_V \lesssim 2 \times 10^{-7}$ so that the total uncertainty $U_T = \sqrt{U_{ST}^2 + U_{1G}^2 + U_V^2}$.

Fig. 1b shows the derivative dI_P/dV_{G2} as a function of V_{G1} and V_{G2} , obtained from a normal-accuracy measurement, following an iterative tuning procedure to find the optimum settings for the DC gate voltages: $(V_{G1}, V_{G2}, V_{G3}, V_{G4}, V_{G5}, V_{G6}) = (-0.96, -0.7, 0.39, -0.78, 0.53, -1)$ V, and $P_{RF} = 5.2$ dBm. During the tuning procedure, plots of $I_P(V_{G1}, V_{G2})$ similar to Fig. 1b were obtained first while systematically stepping V_{G3} and V_{G5} , with the aim of maximising the width of the $1ef$ plateau. At minimum, a 4×4 matrix of (V_{G3}, V_{G5}) values were investigated. Having found the optimal values of V_{G3} and V_{G5} , the procedure was repeated stepping V_{G4} and V_{G6} . Note that the relatively large negative values of the voltages applied to the lower finger gates in Fig. 1a, combined with the positive voltage applied to the plunger gate V_{G3} , has the effect of shifting the QD position above the axis of symmetry defined by the trench gate V_{G5} . The approximate location of the QD is indicated by a dashed red circle in Fig. 1a¹³.

The data of Fig. 1b was taken as a series of V_{G2} scans at fixed V_{G1} , with V_{G1} incremented between scans. This plot, known as the 'pump map', shows clearly the regions of zero derivative, where the current is invariant in the two control voltages^{21,22}. The mis-alignment of regions of maximum derivative in successive scans visible in this data also shows that the device operation is affected by a random telegraph signal (RTS) well known to affect

this type of 2-DEG structure^{23,24} and already observed in another sample⁷ with a similar design to the one in this study. Despite the noise, a broad region can be identified on the one-electron plateau where the derivative is zero within the resolution of the data. In the next section, we use high-accuracy measurements to investigate the robustness of current quantization on the one-electron plateau.

III. HIGH-ACCURACY PLATEAU MEASUREMENTS

We made a total of 6 high-accuracy measurement scans as a function of the control parameters V_{G1} , V_{G2} , V_{G3} and P_{RF} , denoted S1-S6, as well as normal-accuracy measurements over a wider range of each scanned parameter. We also made a further 4 measurements with the pump tuning parameters fixed to the optimal values and $n_{cyc} = 750, 1400, 900$ and 983 , denoted F1-F4. The six scans and four fixed-parameter measurements were made over a period of 14 days. In Fig. 2 we present data from four of the scans, with each set of high-accuracy data plotted (filled circles) on logarithmic (Figs. 2(a-d)) and linear (Figs. 2(e-h)) axes, with normal-accuracy data (open circles) also shown on the logarithmic plots. Each high-accuracy data point in the data of Fig. 2 is averaged from 70 on-off cycles. The error bars indicate the statistical uncertainty $U_{ST} \sim 2 \times 10^{-6}$, which for these relatively short averaging times is the largest component of the total uncertainty; $U_T \sim U_{ST}$. The normal-accuracy data has sufficient accuracy and signal-to-noise ratio to resolve relative deviations of ΔI_P from ef as small as 10^{-4} , and the logarithmic plot is a useful way to visualize the data during the iterative gate tuning procedure. In each scan plotted in Fig. 2, the fixed parameters were set to the optimum values noted in section II. Two additional scans were performed, S1 and S2 (not shown in Fig. 2), with one fixed parameter slightly offset from the optimum: S1 was a V_{G2} scan, with $V_{G1} = -0.975$ V, and S2 was a V_{G1} scan with $V_{G2} = -0.695$ V.

The effect of RTS noise can be seen in the normal-accuracy data, particularly for scan S3, where individual RTS switching events are indicated by gray arrows in Fig. 2a. Nevertheless, for each scan, the high-accuracy data exhibits a plateau where ΔI_P appears invariant in the control parameter within the uncertainty of the individual data points. Scans S3 and S4 can immediately be compared with similar data measured using an etch-defined pump¹¹, and we note that the plateaus in our gate defined pump are approximately twice as wide in both entrance gate (V_{G1}) and exit gate (V_{G2}) as those in the etch-defined pump. This may reflect a higher charging energy of the gate-defined pump, but it could also be an artifact of different lever arms (gate voltage to QD energy conversion factors) resulting from the very different geometries of the two types of device. Comparing scans S4 and S5 (Fig. 2f,g) the effect of the different lever arms

of V_{G2} and V_{G3} on the QD level is clear: both of these gates control the depth of the QD, so I_P has a similar functional dependence on either gate, but because V_{G3} is coupled much more strongly to the QD than V_{G2} , the plateau occupies a smaller range of gate voltage.

To evaluate the plateau extension more quantitatively, two methods were used. Firstly (the 'exponential fit method'), we fitted the high-accuracy data $I_P(x)$ to a sum of two exponential functions¹⁵

$$\frac{I_{FIT}}{ef} = 1 + \delta_I - e^{-\alpha_1(x-x_1)} + e^{\alpha_2(x-x_2)} \quad (1)$$

where α_1 , α_2 , x_1 , x_2 , δ_I are fitting parameters. The parameter δ_I is the best-fit offset of the plateau from ef . We include it because we do not assume *a priori* that the plateau is exactly quantised. For runs S1-S6, we found $0.23 \times 10^{-6} \leq \delta_I \leq 1.33 \times 10^{-6}$. For runs S3 and S6, only the second exponential term was used for the fit because the data had no clear deviation from the plateau on the low-x axis side. We defined the plateau width as the range of the control parameter for which $|(I_{FIT}/ef) - 1 - \delta_I| \leq \delta_{fit}$, with $\delta_{fit} = 10^{-7}$. This choice of δ_{fit} reflects the lower limit to the statistical uncertainty achievable for realistic measurement times of order 1 day. Other studies^{8,11} used the same method to define the plateau, but without including the offset δ_I , and with $\delta_{fit} = 10^{-8}$. The fits are shown in the lower panels of Fig. 2 as solid lines²⁵, and the resulting selections of data points (number of points = N_{exp}) are enclosed by a solid box. The standard deviation of the N_{exp} data points in each scan is denoted $\sigma(\Delta I_P)$, and the statistical uncertainty of ΔI_P averaged over these points on the plateau is $U_{ST,plat} = \sigma(\Delta I_P)/\sqrt{N_{exp}}$. The scatter of the data points inside the boxes appears to be consistent with their individual uncertainties, but we will address this point more quantitatively in section IV.

Secondly, a purely empirical criterion was used, based on linear fits to sections of the high-accuracy data (the 'linear fit method'). This method does not make any assumptions about the functional form of the data. For each scan, we found the largest number N_{lin} of consecutive data points for which $|S| < U_{SLOPE}$, where S is slope of a linear fit to the N_{lin} points, and U_{SLOPE} is the uncertainty in the slope²⁶. The resulting data ranges are enclosed by dashed boxes in the lower panels of Fig. 2, and the relevant parameters are shown in table 1. As with the exponential fit method, the statistical uncertainty of the averaged points is given by $U_{ST,plat} = \sigma(\Delta I_P)/\sqrt{N_{lin}}$. The linear fit method allows us to assign a numerical value to the plateau flatness given by U_{SLOPE} multiplied by the plateau width. The flatness is comparable to the uncertainty of the data points from which it is derived, because the scatter of the data points determines the uncertainty in the linear regression. The flatness therefore is roughly between 1×10^{-6} and 2×10^{-6} for all the scans irrespective of the plateau width in the scanned units. For example, scans S4 and S5 have plateau widths in gate voltage units differing by roughly a factor 3 due to the

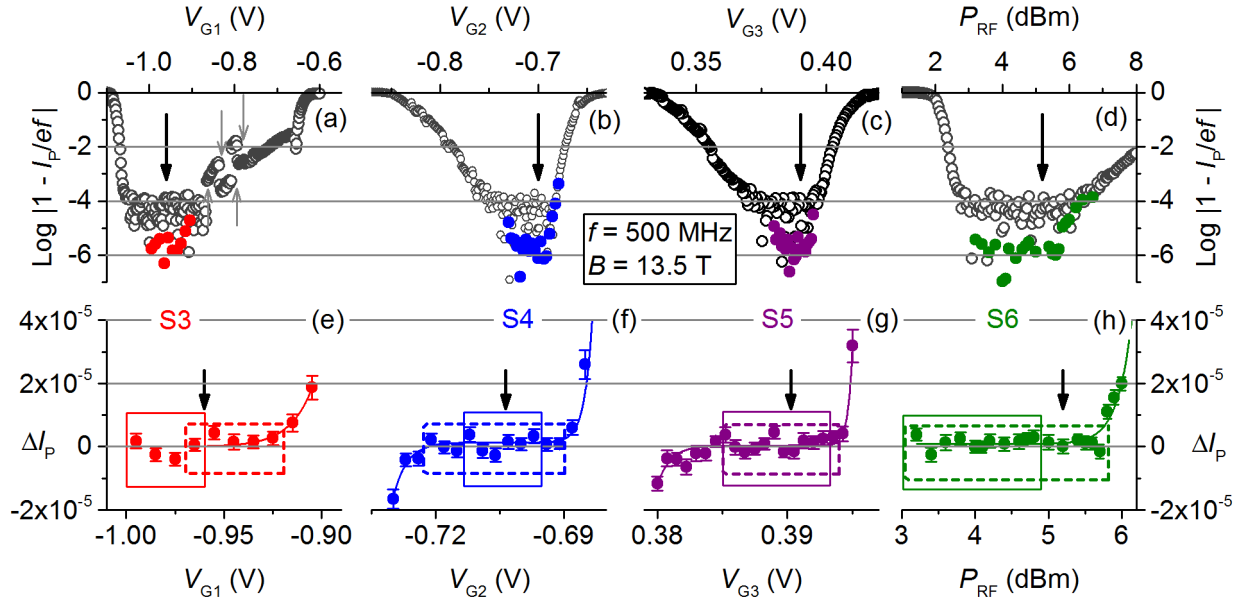


FIG. 2. Pumped current at $f = 500$ MHz and $B = 13.5$ T as a function of four control variables (left to right) V_{G1} , V_{G2} , V_{G3} , and P_{RF} . The upper panels (a-d) show normal-accuracy (open circles) and high-accuracy (filled circles) data on a log scale. Lower panels (e-h) show the same high-accuracy data as the upper panels, on a linear scale with error bars indicating the statistical uncertainty. Solid lines in the lower plots are fits to equation 1. Boxes show the range of data for which a plateau can be defined: solid boxes by reference to the exponential fit lines of equation 1, and dashed boxes by reference to linear fits (linear fit lines are not shown). Thick vertical arrows on all the plots indicate the optimum values of tuning parameters $(V_{G1}, V_{G2}, V_{G3}) = (-0.96, -0.7, 0.39)$ V, and $P_{RF} = 5.2$ dBm. The thin vertical arrows in panel (a) indicate RTS events.

TABLE I. Fit and slope parameters

Scan number	Scanned variable	n_{cyc}	N_{exp}	N_{lin}	plateau width	Slope S $\times 10^{-6}$	U_{SLOPE} $\times 10^{-6}$	Flatness $\times 10^{-6}$
S1	V_{G2}	25	15	21	40 mV	74 /V	81 /V	3.24
S2	V_{G1}	70	6	11	100 mV	19 /V	23.7 /V	2.37
S3	V_{G1}	70	4	5	40 mV	18 /V	53 /V	2.12
S4	V_{G2}	70	6	11	30 mV	24 /V	59 /V	1.77
S5	V_{G3}	70	11	12	8.25 mV	233 /V	261 /V	2.15
S6	P_{RF}	70	11	17	2.5 dBm	-0.22 /dBm	0.51 /dBm	1.27

different lever arms of V_{G2} and V_{G3} as noted above, but the flatness for both the plateaus is $\sim 2 \times 10^{-6}$. To evaluate the flatness with 10^{-7} uncertainty using the linear fit method would require long averaging times, but we note that this is the only unambiguous method of proving that a plateau is flat. The exponential fit method, on the other hand, allows the plateau extension to be estimated based on a much shorter measurement, under the strong assumption that the fitting function (in this case, an exponential) captures all of the physics relevant to the pump accuracy at the target level of uncertainty.

For all the scans, $N_{exp} < N_{lin}$, which is to be expected since we chose $\delta_{fit} \ll U_{ST}$; the exponential fit method estimates the plateau extension to be smaller than the lin-

ear fit method, because the latter is only constrained by $U_{ST} \sim 2 \times 10^{-6}$. For scan S3, scatter of some of the data points strongly constrained the range of points which satisfied the linear fit criterion. As can be seen from table I, a similar scan, S2, exhibited a plateau in V_{G1} more than twice as wide in gate voltage. The question of whether the scatter in run S3 is excessively large is addressed in section IV. Regarding the P_{RF} scan S6, there are some indications in Fig. 2h that an exponential function does not adequately describe the increase of the current for $P_{RF} > 5.7$ dBm, and we speculate that rectification²⁷ or heating may play a role in the breakdown of quantised pumping at large gate drive amplitudes.

The current averaged over the plateaus, with the

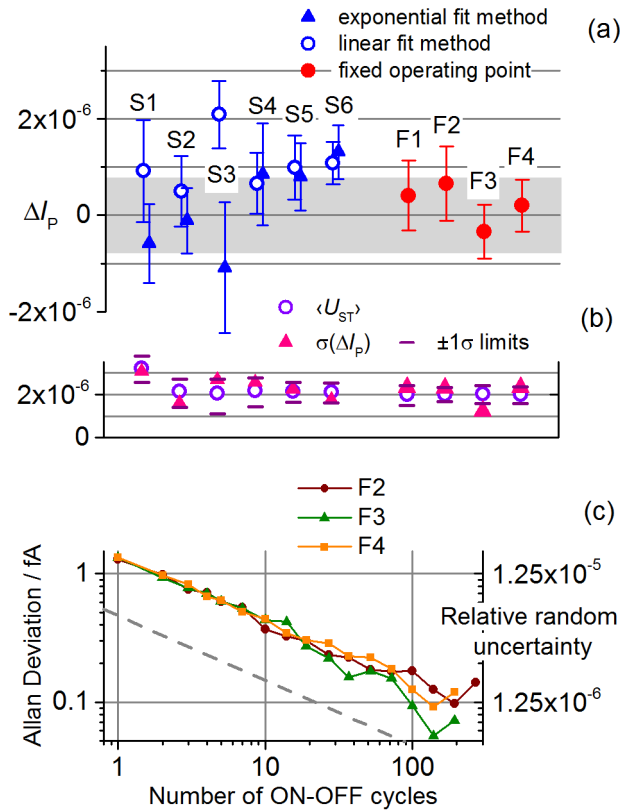


FIG. 3. (a): Average pumped current at $f = 500$ MHz and $B = 13.5$ T obtained from each experimental run, with the run number indicated above the data points. The error bars are the sum of the un-correlated uncertainty components $\sqrt{U_{ST,plat}^2 + U_V^2}$ for scans S1-S6, and $\sqrt{U_{ST}^2 + U_V^2}$ for fixed-points runs F1-F4. The uncertainty in the resistor calibration, $U_{1G} = 8 \times 10^{-7}$, is shown as a shaded grey box. For scans S1-S6, the plotted value is an average over a range of a control parameter, with the range selected using the linear fit method (open circles) and exponential fit method (filled triangles). (b): Statistical properties of the data in plot (a). Data points corresponding to the same run are aligned vertically in (a) and (b). Open circles show the mean U_{ST} for the data points on-plateau, as selected by the exponential fit method for runs S1-S6. For runs F1-F4, they show the mean U_{ST} for the data set analyzed in blocks of 70 on-off cycles. Filled triangles show the standard deviation of the data points on-plateau, and for runs F1-F4 the standard deviation of the data analyzed in blocks of 70 cycles. Horizontal bars show the 68% coverage upper and lower bounds for N_{exp} measurements of ΔI_P to have a given standard deviation, assuming that ΔI_P is normally distributed with standard deviation $\langle U_{ST} \rangle$. (c): Allan deviation of pumped current as a function of the number of on-off cycles, calculated from 3 of the runs at fixed operating point. The Allan deviation for run F1 (not shown) exhibited similar behavior. The gray dashed line shows the expected $1/\sqrt{i}$ dependence for frequency-independent Johnson-Nyquist noise in the reference resistor.

plateaus defined using both the exponential (closed triangles) and linear (open circles) fit methods, is plotted in Fig. 3a for runs S1-S6. Error bars show the un-correlated uncertainty $\sqrt{U_{ST,plat}^2 + U_V^2}$. The current measured in runs F1-F4 with the pump at fixed operating point is also plotted on the same graph (closed circles), with error bars indicating $\sqrt{U_{ST}^2 + U_V^2}$. The un-correlated uncertainty does not include U_{1G} , which is shown as a grey box centred on $\Delta I_P = 0$. The resistor was calibrated before and after the measurement campaign and its value was assumed constant during the campaign based on its long-term drift rate of $\sim 0.01(\mu\Omega/\Omega)/\text{day}^5$. In contrast, the voltage measurement was calibrated before and after each run. The un-correlated uncertainty thus allows the different measurements of ΔI_P to be compared with each other without the additional uncertainty associated with linking to the SI unit system. For example, the two fixed-point runs with the lowest uncertainty, F3 and F4, are consistent within their combined uncertainty of 7.8×10^{-7} . If the plateau is defined using the exponential fit method, the average current is consistent with ef within the uncertainties, and furthermore there are no major inconsistencies between the data points when only the un-correlated uncertainty is considered. Averaging all the data from the four fixed-point runs (a total of 4033 cycles lasting 47 hours) reduced U_{ST} such that $U_T \sim U_{1G}$ and yielded a best estimate of the pump current: $\Delta I_P = 0.28 \pm 0.86 \times 10^{-6}$. This is marginally more accurate than the previous best electron pump measurement using the current measurement system at NPL⁹, although it falls short of the record low uncertainty of 1.6×10^{-7} recently reported¹¹ using a measurement system based on a new type of ultra-stable current preamplifier known as an 'ULCA'⁶. Future efforts will aim to reduce U_{1G} to around 2×10^{-7} as well as implementing an ULCA-based measurement system at NPL. It is interesting to note that the accumulated precision measurements and associated theoretical fit lines^{5,7-9,11}, suggest that a tunable-barrier electron pump operated at an optimal working point is accurate at the 1×10^{-7} level. With this premise, we could hypothetically consider the pump as a primary current standard, and the data of runs F1-F4 as constituting a calibration of the reference resistor with total uncertainty $\sim 3 \times 10^{-7}$, almost a factor 3 lower than the U_{1G} presently achievable at NPL. However, we believe such a step would be premature, and that the robustness of these pumps requires further extensive investigation before a consensus can be reached on the required set of conditions for operation at a given accuracy level.

IV. STATISTICAL EVALUATION OF PLATEAU CURRENT

The data points on the plateaus in Fig. 2 show some scatter, and we now evaluate whether this scatter is con-

sistent with statistical scatter about a stationary mean or whether it is a sign of structure on the plateau, or possibly drift in the pump current or the measurement system. We note that recent developments in the metrology of small currents^{6,28} have focused attention on the stability of high-value thick-film standard resistors, principally those of 100 M Ω value. The 1 G Ω standard resistor used in the reference current source is also a thick-film design, and may suffer from short-term instability at the sub-ppm level. However, the uncertainties in the data of Figs. 2 and 3 are too large for this to have a significant effect on the scatter of the data points. We focus on the more conservative (narrower) plateaus defined using the exponential fit method. For each scan, the mean of the N_{exp} values of the statistical uncertainty U_{ST} , denoted $\langle U_{\text{ST}} \rangle$, is plotted as the open points in Fig 3b. We also plot as solid points the standard deviation $\sigma(\Delta I_{\text{P}})$ of the N_{exp} values of ΔI_{P} . If the current on the plateau was drifting on the time-scale of the scan, or if the plateau was not flat, we expect $\sigma(\Delta I_{\text{P}}) > \langle U_{\text{ST}} \rangle$. To assign a statistical significance to the ratio $\sigma(\Delta I_{\text{P}})/\langle U_{\text{ST}} \rangle$, we used a numerical simulation to assign a 68% confidence interval to the distribution of $\sigma(\Delta I_{\text{P}})$ expected for N_{exp} normally-distributed measurements with standard deviation $\langle U_{\text{ST}} \rangle$ ²⁹. This is plotted as upper and lower horizontal bars in Fig. 3b. The fixed-parameter runs F1-F4 were evaluated in the same way as the scans, by dividing the data into blocks of 70 cycles and analyzing each block separately. Over the whole data set, there is no statistically significant deviation of the ratio $\sigma(\Delta I_{\text{P}})/\langle U_{\text{ST}} \rangle$ from 1. One particular run, S3, appeared to have anomalously large scatter, visible in Fig. 2(e) and already discussed in section III. This scatter is apparent in Fig. 3(b), in the relatively large ratio of $\sigma(\Delta I_{\text{P}})/\langle U_{\text{ST}} \rangle$. However, $\sigma(\Delta I_{\text{P}})$ is still just within the 68% confidence interval, clarifying that the data at different $V_{\text{G}1}$ values cannot be distinguished from data drawn from the same distribution. Overall, we conclude from this analysis that the scatter of the data points on the plateaus is consistent with statistical fluctuations about a stationary mean.

This conclusion is supported by the Allan deviation of the current measured from runs F1-F4, all of which exhibited similar behavior. The Allan deviation plots for runs F2-F4 are shown in Fig. 3c. They show no significant deviation from the expected \sqrt{t} behavior for frequency-independent noise out to the longest averaging times probed by the Allan deviation analysis³⁰, roughly one quarter of the total measurement time, or ~ 3 hours. For comparison, the dashed line shows the expected Allan deviation of frequency independent Johnson-Nyquist noise in the 1 G Ω resistor, $(4.2 \text{ fA}/\sqrt{\text{Hz}})/(\sqrt{2\tau})$, where $\tau = 40$ s is the time for one on-off cycle. The Allan deviation of the pump current is increased above this theoretical level due to three inefficiencies in the duty cycle which reduce the effective averaging time: The on-off cycle means the pump current is only measured for half the time, auto zero in the readout voltmeters halves the measurement time again, and rejection of data points

at the start of each half-cycle, to eliminate transient effects, further reduces the duty cycle. The latter two of these effects need to be optimized in future experiments to yield a lower overall statistical uncertainty¹¹.

V. PUMPING REGIME AND NOISE BROADENING

The relatively high temperature of these measurements compared to previous high-precision studies motivated us to consider the mechanism of charge capture by the pump. At low temperatures, this occurs by a cascade of one-way tunneling events whereby electrons tunnel back to the source electrode as the QD is progressively isolated from the source^{4,31}. The experimental signature of the decay cascade is a characteristic double-exponential shape to the pump current as a function of the QD depth-tuning parameter. This tuning parameter can be the 'exit gate' voltage in simple two-gate pumps^{5,8,14}, or a global top gate voltage^{9,31}, and in this work its role can be fulfilled by either $V_{\text{G}2}$ or $V_{\text{G}3}$. At higher temperatures, experimental¹⁶ and theoretical^{15,32} work has indicated a cross-over to a thermal regime, in which back-tunneling is accompanied by forward tunneling into the QD from the source. This results in a symmetric shape to the current as a function of QD depth tuning parameter, reflecting the Fermi distribution of electrons in the leads. The cross-over to the thermal regime has been predicted to occur for $10 \times k_{\text{B}}T \gtrsim \Delta_{\text{ptb}}$ ¹⁵. Here, Δ_{ptb} is defined as the change in energy of the QD level when the entrance barrier transmission changes by a factor of Euler's number $\sim 2.718\dots$ and it thus quantifies the device-specific cross coupling between the modulated entrance barrier, and the QD energy level³². We crudely estimate $\Delta_{\text{ptb}} \sim 1 \text{ meV} = 8.9 \times k_{\text{B}}T$ for our device, based on the slope of representative conductance pinch-off data and typical lever arm factors between a gate voltage and QD energy level. From this estimate we expect the device to be between the two regimes, and we next examine experimental data to clarify the capture mechanism.

In Fig. 4a, we plot the normalized pump current as a function of $V_{\text{G}3}$, which functions as a QD depth-tuning gate. A RTS is visible in the transition between the plateaus, where the pump current is a sensitive probe of changes in the electrostatic potential. On the plateau, the current is insensitive to the state of the RTS. For the data of Fig. 4a, in the transition region between $I_{\text{P}} = 0$ and $I_{\text{P}} = ef$, the charge state causing the RTS noise appears to be in one state for the majority of the data points (filled points), and the points affected by a switch to the other state (open points) were excluded from fitting. The data is fitted to the decay cascade model⁴:

$$\frac{I_{\text{P}}}{ef} = \sum_{m=1}^2 \exp(-\exp(-aV_{\text{G}3} + \Delta_m)) \quad (2)$$

over the full range (solid line), with reduced $\chi^2 = 2.6 \times$

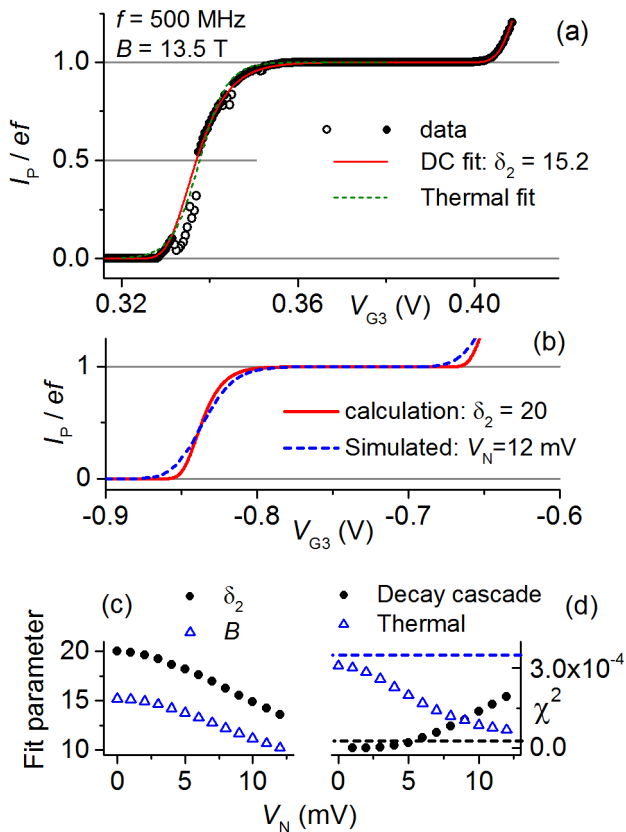


FIG. 4. (a): Open and filled points: normalized pump current as a function of V_{G3} measured using the normal-accuracy method. $f = 500$ MHz, $B = 13.5$ T and $P_{RF} = 5.2$ dBm. Solid line: fit of equation (2) to the filled points. Dashed line: fit of equation (3) to the filled points. Open points denote data excluded from the fits. (b): Plot of equation (2) (solid line) and after simulated broadening by Gaussian noise with standard deviation 12 mV (dashed line). (c) and (d) show fit parameters (c) and Chi-Square (d) as a function of noise amplitude for fits of equations (2) (filled circles) and (3) (open triangles) to simulated noise-broadened data similar to that shown as the dashed line in plot (b).

10^{-5} , yielding the fit parameter $\delta_2 \equiv (\Delta_2 - \Delta_1) = 15.2$, and a thermal equilibrium (Fermi function) model^{16,32}:

$$\frac{I_P}{ef} = \frac{1}{1 + e^{(A - V_{G3})/B}} \quad (3)$$

in the range $0.32 \leq V_{G3} \leq 0.38$ (dotted line) with reduced $\chi^2 = 3.5 \times 10^{-4}$. Close inspection of the fit lines shows that the decay-cascade model gives a better fit, and the thermal equilibrium model fails to reproduce the asymmetric plateau shape, with a sharp riser from $I_P = 0$ and a more gradual approach to $I_P = ef$. The reduced χ^2 for the decay-cascade fit is more than a factor 10 smaller than the thermal equilibrium fit, suggesting that the pump is operating in the decay cascade regime.

A similar conclusion was drawn by fitting equations (2) and (3) to a $I_P(V_{G2})$ scan³³ which was obtained with a faster sweep rate to the data of Fig 4(a). This data was not so much affected by RTS switching events, at the expense of a much smaller number of data points (~ 15) in the region between $I_P = 0$ and $I_P = ef$. For this data, equation (2) yielded $\delta_2 = 15.6$ with $\chi^2 = 2.6 \times 10^{-4}$ and equation (3) yielded a fit with $\chi^2 = 6.0 \times 10^{-4}$.

The high RF power levels used in this experiment, corresponding to on-chip peak-to-peak gate voltages of order 1 V, raise the possibility that the electron temperature in the leads is elevated from the refrigerator bath temperature, for example by RF currents from the entrance gate flowing to ground through stray capacitances and parts of the leads. We did not estimate the electron temperature in the leads, but some insight can be gained by cooling the device to 300 mK. If RF-induced heating was the dominant mechanism determining the electron temperature at a bath temperature of 1.3 K, we would not expect further reduction of the bath temperature to have any effect on the device characteristics. In fact, we observe a considerable sharpening of the plateau when the device is cooled to 300 mK; fits of $I_P(V_{G2})$ to equation (2) yield $\delta_2 \sim 20$, compared to $\delta_2 \sim 15$ at 1.3 K³⁴. We can conclude that RF-induced heating is not a dominant mechanism determining the device characteristics at a bath temperature of 1.3 K, although it may play a role at 300 mK.

We also rule out the possibility that the data of Fig. 4a is broadened by noise leading to erroneous conclusions from the fits. We calculated numerically the effect of Gaussian fluctuations in V_{G3} , with standard deviation V_N , on the ideal decay-cascade behavior described by equation (2). Fig. 4b shows eq. (2) with $\delta_2 = 20$ (solid line), and after broadening with $V_N = 12$ mV (dotted line). The broadened characteristic is more symmetric and resembles a thermal distribution. Fitting the noise-broadened characteristic to the decay-cascade formula results in a decreasing δ_2 parameter as V_N is increased (Fig. 4c, solid symbols), but also a progressive reduction in the quality of the fit, reflected in an increase in χ^2 (Fig. 4d, solid symbols). Fitting to the thermal function, eq. (3), the reverse is true: the thermal fit becomes a more accurate description of the simulated data for larger noise amplitudes (Fig. 4d, open symbols). Comparing the actual χ^2 values obtained from fitting the data of Fig. 4(a) (horizontal dashed lines in Fig. 4(d)) with those calculated from noise broadening, we conclude that the experimentally measured data is not consistent with more than a few mV of noise broadening, and the pump is indeed operating in the decay cascade regime at our experimental temperature.

VI. CONCLUSIONS

In conclusion, pumping in a GaAs tunable-barrier electron pump is robust against changes in the gate control

parameters, and the RF drive amplitude, at the part-per-million level at a temperature of 1.3 K. The presence of two-level fluctuators did not affect the accuracy of the pump current. Compared to previous studies, this relaxes the experimental conditions required to observe quantised pumping at the part-per-million accuracy level, which is a promising step towards adoption of quantised charge pumps as current standards.

ACKNOWLEDGMENTS

This research was supported by the UK department for Business, Energy and Industrial Strategy, the Joint Research Project 'Quantum Ampere' (JRP SIB07) within the European Metrology Research Programme (EMRP) and the EMPIR Joint Research Project 'e-SI-Amp' (15SIB08). The EMRP is jointly funded by the EMRP participating countries within EURAMET and the European Union. The European Metrology Programme for Innovation and Research (EMPIR) is co-financed by the Participating States and from the European Union's Horizon 2020 research and innovation programme. The study was partially supported by the Korea Research Institute for Standards and Science (16011245) and the national Research Foundation of Korea (NRF-2016R1A5A1008184 and NRF-2016K1A3A7A03951913).

REFERENCES

- ¹J. P. Pekola, O.-P. Saira, V. F. Maisi, A. Kemppinen, M. Möttönen, Y. A. Pashkin, and D. V. Averin, "Single-electron current sources: Toward a refined definition of the ampere," *Reviews of Modern Physics* **85**, 1421 (2013).
- ²M. W. Keller, J. M. Martinis, N. M. Zimmerman, and A. H. Steinbach, "Accuracy of electron counting using a 7-junction electron pump," *Applied Physics Letters* **69**, 1804 (1996).
- ³B. Kaestner and V. Kashcheyevs, "Non-adiabatic quantized charge pumping with tunable-barrier quantum dots: a review of current progress," *Reports on Progress in Physics* **78**, 103901 (2015).
- ⁴V. Kashcheyevs and B. Kaestner, "Universal decay cascade model for dynamic quantum dot initialization," *Physical Review Letters* **104**, 186805 (2010).
- ⁵S. P. Giblin, M. Kataoka, J. D. Fletcher, P. See, T. Janssen, J. P. Griffiths, G. A. C. Jones, I. Farrer, and D. A. Ritchie, "Towards a quantum representation of the ampere using single electron pumps," *Nature Communications* **3**, 930 (2012).
- ⁶D. Drung, C. Krause, U. Becker, H. Scherer, and F. J. Ahlers, "Ultrastable low-noise current amplifier: A novel device for measuring small electric currents with high accuracy," *Review of Scientific Instruments* **86**, 024703 (2015).
- ⁷M.-H. Bae, Y.-H. Ahn, M. Seo, Y. Chung, J. D. Fletcher, S. P. Giblin, M. Kataoka, and N. Kim, "Precision measurement of a potential-profile tunable single-electron pump," *Metrologia* **52**, 195 (2015).
- ⁸F. Stein, D. Drung, L. Fricke, H. Scherer, F. Hohls, C. Leicht, M. Goetz, C. Krause, R. Behr, E. Pesel, U. Siegner, F.-J. Ahlers, and H. W. Schumacher, "validation of a quantized-current source with 0.2 ppm uncertainty," *Applied Physics Letters* **107**, 103501 (2015).
- ⁹G. Yamahata, S. P. Giblin, M. Kataoka, T. Karasawa, and A. Fujiwara, "Gigahertz single-electron pumping in silicon with an accuracy better than 9.2 parts in 10^7 ," *Applied Physics Letters* **109**, 013101 (2016).
- ¹⁰F. Stein, T. Gerster, R. Behr, M. Gotz, E. Pesel, T. Weimann, K. Pierz, H. W. Schumacher, and F. Hohls, "Accuracy verification of single-electron pumps with 0.2 ppm uncertainty," in *2016 Conference on Precision Electromagnetic Measurements (CPEM 2016)* (IEEE, 2016).
- ¹¹F. Stein, H. Scherer, T. Gerster, R. Behr, M. Götz, E. Pesel, C. Leicht, N. Ubbelohde, T. Weimann, K. Pierz, *et al.*, "Robustness of single-electron pumps at sub-ppm current accuracy level," *Metrologia* **54**, S1 (2016).
- ¹²F. Stein, R. Behr, M. Gotz, E. Pesel, T. Weimann, K. Pierz, H. Schumacher, and F. Hohls, "Robustness of single-electron pumps at sub-ppm level," in *2016 Conference on Precision Electromagnetic Measurements (CPEM 2016)* (IEEE, 2016).
- ¹³M. Seo, Y.-H. Ahn, Y. Oh, Y. Chung, S. Ryu, H.-S. Sim, I.-H. Lee, M.-H. Bae, and N. Kim, "Improvement of electron pump accuracy by a potential-shape-tunable quantum dot pump," *Physical Review B* **90**, 085307 (2014).
- ¹⁴S. P. Giblin, S. J. Wright, J. D. Fletcher, M. Kataoka, M. Pepper, T. J. B. M. Janssen, D. A. Ritchie, C. A. Nicoll, D. Anderson, and G. A. C. Jones, "An accurate high-speed single-electron quantum dot pump," *New Journal of Physics* **12**, 073013 (2010).
- ¹⁵V. Kashcheyevs and J. Timoshenko, "Modeling of a tunable-barrier non-adiabatic electron pump beyond the decay cascade model," in *Precision Electromagnetic Measurements (CPEM 2014), 2014 Conference on* (IEEE, 2014) pp. 536–537.
- ¹⁶G. Yamahata, K. Nishiguchi, and A. Fujiwara, "Accuracy evaluation and mechanism crossover of single-electron transfer in si tunable-barrier turnstiles," *Physical Review B* **89**, 165302 (2014).
- ¹⁷S. J. Wright, M. D. Blumenthal, G. Gumbs, A. L. Thorn, M. Pepper, T. Janssen, S. N. Holmes, D. Anderson, G. A. C. Jones, C. A. Nicoll, *et al.*, "Enhanced current quantization in high-frequency electron pumps in a perpendicular magnetic field," *Physical Review B* **78**, 233311 (2008).
- ¹⁸B. Kaestner, C. Leicht, V. Kashcheyevs, K. Pierz, U. Siegner, and H. W. Schumacher, "Single-parameter quantized charge pumping in high magnetic fields," *Applied Physics Letters* **94**, 012106 (2009).

- ¹⁹J. D. Fletcher, M. Kataoka, S. P. Giblin, S. Park, H.-S. Sim, P. See, D. A. Ritchie, J. P. Griffiths, G. A. C. Jones, H. E. Beere, and T. J. B. M. Janssen, “Stabilization of single-electron pumps by high magnetic fields,” *Physical Review B* **86**, 155311 (2012).
- ²⁰See supplementary figure S1.
- ²¹M. D. Blumenthal, B. Kaestner, L. Li, S. P. Giblin, T. J. B. M. Janssen, M. Pepper, D. Anderson, G. A. C. Jones, and D. A. Ritchie, “Gigahertz quantized charge pumping,” *Nature Physics* **3**, 343–347 (2007).
- ²²B. Kaestner, V. Kashcheyevs, G. Hein, K. Pierz, U. Siegner, and H. W. Schumacher, “Robust single-parameter quantized charge pumping,” *Applied Physics Letters* **92**, 192106 (2008).
- ²³D. Cobden, N. Patel, M. Pepper, D. Ritchie, J. Frost, and G. Jones, “Noise and reproducible structure in a GaAs/Al_xGa_{1-x}As one-dimensional channel,” *Physical Review B* **44**, 1938 (1991).
- ²⁴F. Liefink, J. Dijkhuis, and H. Van Houten, “Low-frequency noise in quantum point contacts,” *Semiconductor science and technology* **9**, 2178 (1994).
- ²⁵See supplementary figure S1 for an example illustration of the fit line on an expanded y-axis.
- ²⁶An estimate of the uncertainty in the slope is given by the square root of the second diagonal element in the 2×2 covariance matrix output by the fitting algorithm. See standard texts on regression analysis, for example Draper and Smith, *Applied Regression Analysis* (second edition), Wiley (1981), pp 82-85.
- ²⁷S. P. Giblin, M. Kataoka, J. D. Fletcher, P. See, T. J. B. M. Janssen, J. P. Griffiths, G. A. C. Jones, I. Farrer, and D. A. Ritchie, “Rectification in mesoscopic alternating current-gated semiconductor devices,” *Journal of Applied Physics* **114**, 164505 (2013).
- ²⁸D. Drung, C. Krause, S. P. Giblin, S. Djordjevic, F. Piquemal, O. Séron, F. Renguez, M. Götz, E. Pesel, and H. Scherer, “Validation of the ultrastable low-noise current amplifier as travelling standard for small direct currents,” *Metrologia* **52**, 756 (2015).
- ²⁹See supplementary information for more detail on the statistical analysis.
- ³⁰D. W. Allan, “Should the classical variance be used as a basic measure in standards metrology?” *IEEE Transactions on instrumentation and measurement* **1001**, 646–654 (1987).
- ³¹A. Fujiwara, K. Nishiguchi, and Y. Ono, “Nanoampere charge pump by single-electron ratchet using silicon nanowire metal-oxide-semiconductor field-effect transistor,” *Applied Physics Letters* **92**, 042102 (2008).
- ³²L. Fricke, M. Wulf, B. Kaestner, V. Kashcheyevs, J. Timoshenko, P. Nazarov, F. Hohls, P. Mirovsky, B. Mackrodt, R. Dolata, T. Weimann, K. Pierz, and H. W. Schumacher, “Counting statistics for electron capture in a dynamic quantum dot,” *Physical Review Letters* **110**, 126803 (2013).
- ³³See supplementary figure S3(a).
- ³⁴See supplementary figures S3(a) and (b).

VII. SUPPLEMENTARY INFORMATION

The purpose of this supplementary information is to provide more detail on the analysis process for the high-accuracy measurements (Figure S1), and the calculation of statistical quantities used in the main text (Figure S2). We also show a comparison between exit gate characteristics at two different temperatures (Figure S3), illustrating the sharpening of the plateau when the pump is cooled from 1.3 K to 300 mK.

Figure S1 illustrates the process of analysing raw data. As explained in the main text, the high-accuracy measurement system compares the unknown pump current I_P with a reference current generated by applying a voltage across a calibrated 1 G Ω resistor. The raw data are readings from two instruments: an ammeter which measures the difference between the pump and reference currents (Fig. S1(a)) and a voltmeter which measures the voltage across the 1 G Ω resistor (Fig. S1(b)). The currents are switched on and off synchronously with a cycle time of 40 seconds to remove instrumental offsets. Note that due to careful tuning of the reference current source, the (on-off) ammeter difference signal ~ 10 fA is only just visible in the raw data. In this study, each half-cycle consisted of 50 readings from each instrument, triggered synchronously, with the instruments set to integrate for 10 power line cycles (at a nominal power line frequency of 50 Hz) and including an auto zero measurement with each reading. Thus, each instrument reading takes 0.4 s, each half-cycle takes 20 s and the 70 cycles shown in the figure take 2800 s.

The inset to Fig. 1(a) shows a small portion of the ammeter data from the main panel; the first one and a half on-off cycles. The points are color-coded to illustrate the data analysis procedure. The first 16 data points following each current switch (grey) are rejected to eliminate transient effects. The remaining 34 data points from the *off* half-cycle (green) are averaged to yield I_{OFF} . The 34 points from each *on* half-cycle are divided into two equal portions, and the two blocks of 17 points adjacent to the *off* cycle are averaged to yield I_{ON} . The ammeter difference signal extracted from the illustrated data is $\Delta I(1) = I_{ON} - I_{OFF}$. The first block from the first *on* half-cycle (first section of black points) is discarded altogether, and the second block from the second *on* half-cycle (second section of black points) is analysed with the second *off* half cycle, and the first block from the third *on* half-cycle to yield $\Delta I(2)$, and so on up to $\Delta I(n_{cyc} - 1)$. The voltmeter data is analyzed in a similar way to yield $\Delta V(j)$, with $1 \leq j \leq (n - 1)$, and the pump current is given by $I_P(j) = \Delta V(j)/R + \Delta I(j)^5$. Breaking the data set up in this manner makes the measurement of I_P insensitive to linear drift in the offset of the measured signals, at the expense of discarding data from one on-off cycle. The data analysis thus yields $n_{cyc} - 1$ values of ΔI_P from a raw data set of n_{cyc} cycles (Fig. S1(c)). The mean and standard deviation σ_I of the data of Fig. S1(c) yield one data point in Fig. S1(d) indicated by an arrow,

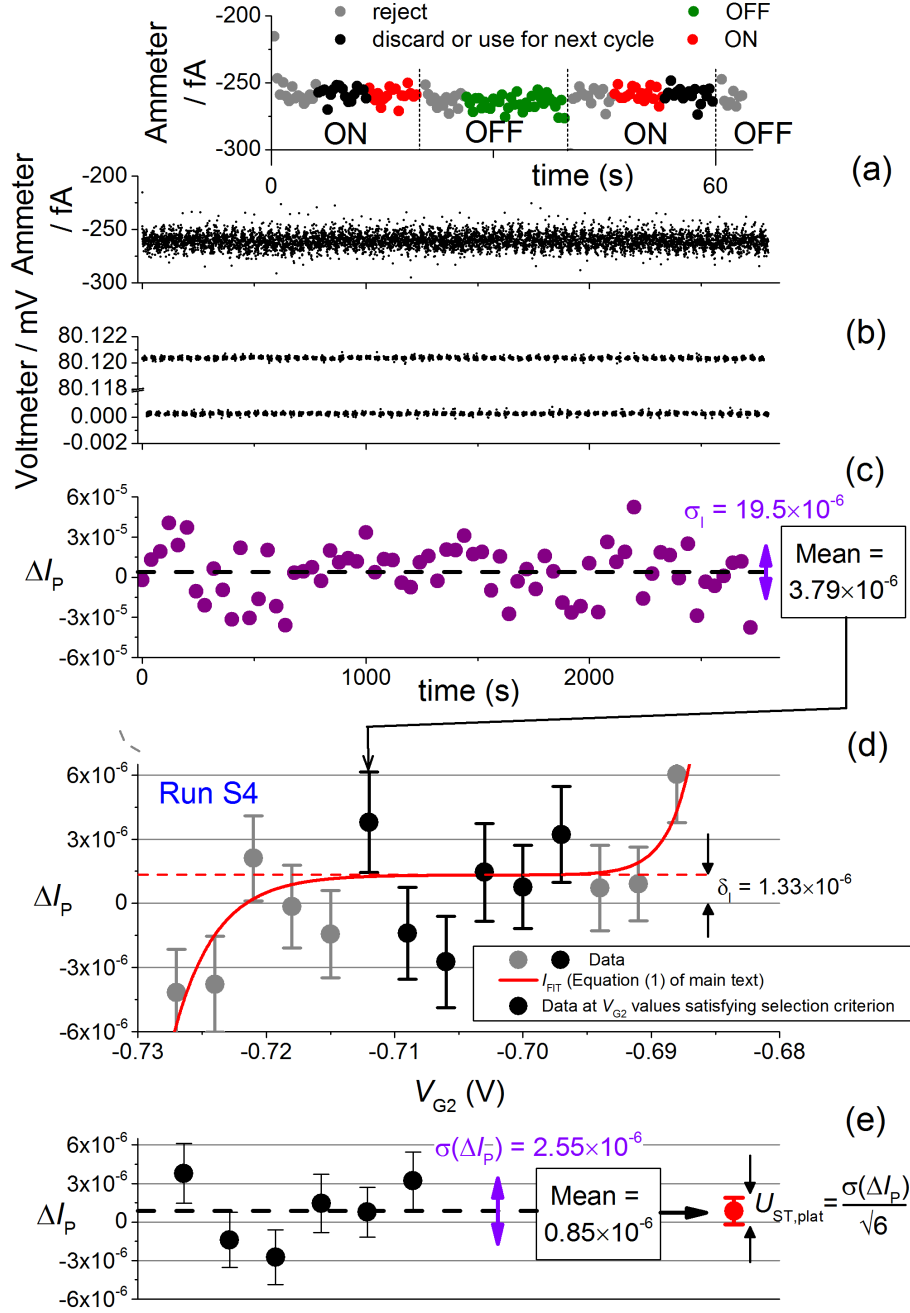


FIG. S1. (a,b): Raw ammeter (a) and voltmeter (b) data. The data shows $n_{cyc} = 70$ on-off cycles from run S4 at $V_{G2} = -0.712$ V. The inset to (a) shows the first ~ 60 s of data with the points color-coded to illustrate the data analysis protocol. The pump and reference current source are turned on and off synchronously every 40 s, indicated by vertical dashed lines. (c): Values of ΔI_P obtained from processing the data raw data from panels (a) and (b). The mean of the $(n_{cyc} - 1) = 69$ points is indicated by a horizontal dashed line, and the standard deviation σ_1 is indicated by the vertical double-arrow. Panels (a)-(c) share the same time axis. (d): Reproduction of Figure 2(f) of the main text, showing scan S4 on an expanded y-axis. The data point indicated by the arrow is averaged from the data points of panel (c). As in Figure 2 of the main text, the error bars are the statistical uncertainty $U_{ST} = \sigma_1 / \sqrt{n_{cyc} - 1}$ and the solid red line shows a fit to equation (1) of the main text. The fitting parameter δ_1 , which is the offset of the fit line from $\Delta I_P = 0$, is indicated on the plot by a horizontal red dashed line. (e): (Black filled circles) Selection of $N_{exp} = 6$ data points from panel (d) at V_{G2} values for which $|(I_{FIT}/ef) - 1 - \delta_1| \leq 1 \times 10^{-7}$. The mean of these 6 data points is indicated by a horizontal dashed line, and the standard deviation by a vertical double arrow. The red data point to the right shows the mean with the error bar indicating statistical uncertainty $U_{ST,plat} = \sigma(\Delta I_P) / \sqrt{N_{exp}}$. This is the same data point plotted as a solid triangle labeled 'S4' in Fig. 3(a) of the main text the error bar is marginally larger because it includes U_V .

with $\Delta I_P = 3.79 \times 10^{-6} \pm U_{ST} = (3.79 \pm 2.33) \times 10^{-6}$. Here, the statistical uncertainty U_{ST} is given by the standard error on the mean $\sigma_I/\sqrt{n_{cyc} - 1}$. For this data point the relative total uncertainty $U_T = \sqrt{U_{ST}^2 + U_{IG}^2 + U_V^2} = 2.47 \times 10^{-6} \sim U_{ST}$.

Referring to the scatter of the data points in Fig. S1(d), we define two more statistical terms, with reference to Fig. S1(e). Here, we have re-plotted the $N_{exp} = 6$ data points in Fig. S1(d) which are determined to be on the *ef* plateau by using the exponential fit method (equation (1) of the main text). The mean of the data points is indicated by a horizontal dashed line. Each of the data points has a statistical uncertainty, and we calculate the mean of these statistical uncertainties, denoted $\langle U_{ST} \rangle = 2.18 \times 10^{-6}$. We also calculate the standard deviation of the 6 data points, denoted $\sigma(\Delta I_P)$, from which we derive the standard error of the mean $= \sigma(\Delta I_P)/\sqrt{N_{exp}} = U_{ST,plat}$. To recap, the symbol U_{ST} denotes the statistical uncertainty for a measurement of ΔI_P at fixed pump operating point, while $U_{ST,plat}$ denotes the statistical uncertainty of an average of several measurements of ΔI_P at different operating points along a plateau.

If the plateau is truly flat, the scatter of the data points on the plateau given by $\sigma(\Delta I_P)$ should be on average the same as the uncertainty U_{ST} of a single data point. In other words, data points measured at different points along the plateau are sampling the same stationary mean value with a standard deviation given by the same underlying noise process. The dominant source of noise in our experiment comes from the measurement system: Johnson noise in the 1 G Ω reference resistor, with additional small contributions from the current pre-amplifier and

cryogenic wiring. This is reflected in the almost constant (within $\sim 10\%$) values of U_{ST} for $n_{cyc} = 70$ visible in Fig. 3(b) (open circles) of the main text. We can therefore state that on a true plateau, data points with $n_{cyc} = 70$ should be drawn from a normal (Gaussian) parent distribution with standard deviation $\langle U_{ST} \rangle$. Since we measure a limited number N_{exp} of data points on the plateau, we can compare the standard deviation $\sigma(\Delta I_P)$ of these points with the expected distribution of the standard deviation, if we randomly selected N_{exp} points from the parent distribution. To do this, we numerically generated a parent distribution with a large number of data points, and randomly selected N_{exp} points from it. The random selection was repeated 10^6 times, and in Fig. S2 (a), we plot the histogram of the $\sigma(\Delta I_P)$ values for $N_{exp} = 6$ and $\langle U_{ST} \rangle = 2.18 \times 10^{-6}$ (the parameters corresponding to run S4, Fig. 2(f) of the main text). The value of $\sigma(\Delta I_P)$ measured for run S4 is shown as a dashed vertical white line super-imposed on the histogram. In the inset to Fig. S2(a) we plot a histogram of $(N - 1)[\sigma(\Delta I_P)]^2/\langle U_{ST} \rangle^2$ (black bars) for the same random data set as the main panel, and for comparison, the χ^2 distribution with 5 degrees of freedom (solid red line). This illustrates a standard text-book result, namely that the variance of N randomly selected points is distributed according to the χ^2 distribution with $N - 1$ degrees of freedom. Fig. S2(b) shows the cumulative sum of the histogram in (a), with vertical dashed lines showing the 1σ (68 % coverage) upper and lower limits to $\sigma(I_P)$. These are plotted as horizontal bars for run S4 in Fig. 3(b) of the main text. The process illustrated in Fig. S2 was repeated with the parameters $[\langle U_{ST} \rangle, N_{exp}]$ for the remaining 5 scans to derive the horizontal bars in Fig. 3(b) of the main text.

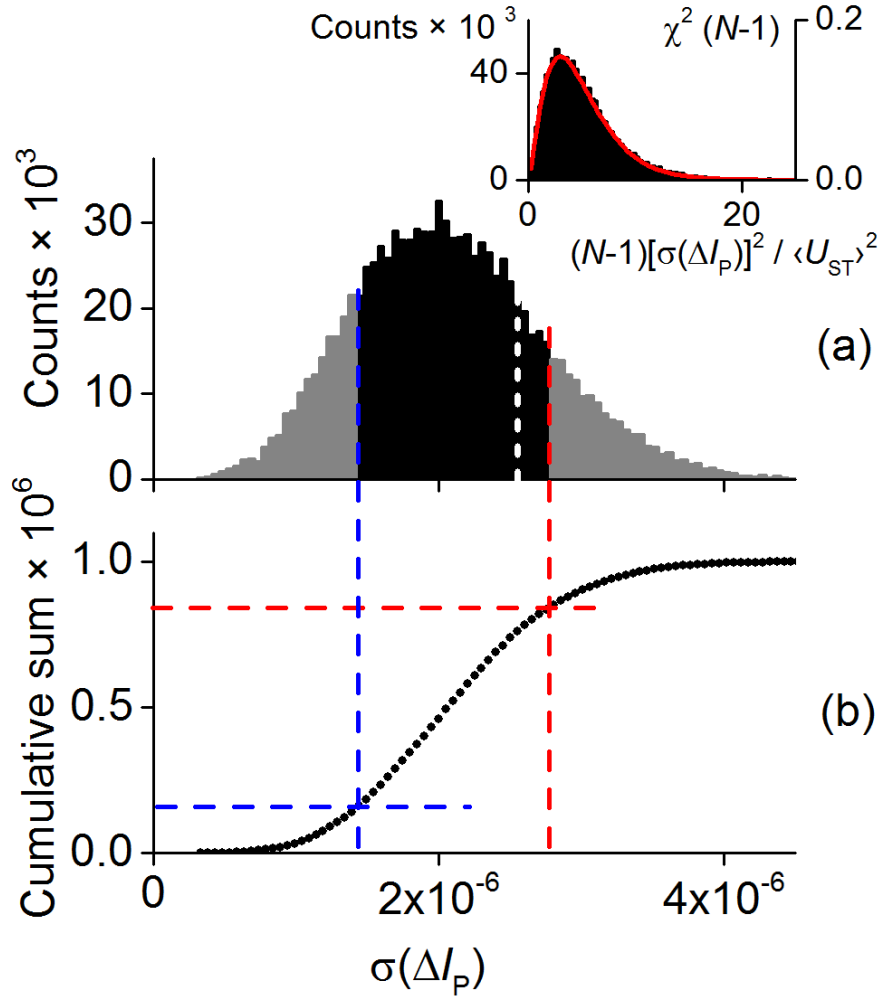


FIG. S2. (a): Histogram of the standard deviation $\sigma(\Delta I_P)$ of $N_{\text{exp}} = 6$ data points randomly selected from a numerically generated normal distribution with standard deviation $\langle U_{\text{ST}} \rangle = 2.18 \times 10^{-6}$. The parameters $[\langle U_{\text{ST}} \rangle, N_{\text{exp}}]$ correspond to the data points within the solid box for run S4 (Fig. 2f of the main text), and the standard deviation $\sigma(\Delta I_P)$ for run S4 is shown as a white vertical dashed line. The random selection was repeated 10^6 times. (b): cumulative sum of the histogram in (a). Horizontal dashed lines demarcate the conventional $1 - \sigma$ upper and lower boundaries, and the intersection of these lines with the data gives the upper and lower $1 - \sigma$ boundaries for a sample of 6 points having a given standard deviation. These boundaries are indicated by vertical dashed lines which are extended up to plot (a), where the histogram bars are color-coded black (inside the $1 - \sigma$ boundary) or gray (outside the $1 - \sigma$ boundary). The inset to (a) (black bars, left y-axis) shows $(N - 1)[\sigma(\Delta I_P)]^2 / \langle U_{\text{ST}} \rangle^2$, with $N = 6$, for the same simulation data as the main panel. The solid red line (right y-axis) shows the χ^2 distribution with $(N - 1) = 5$ degrees of freedom.

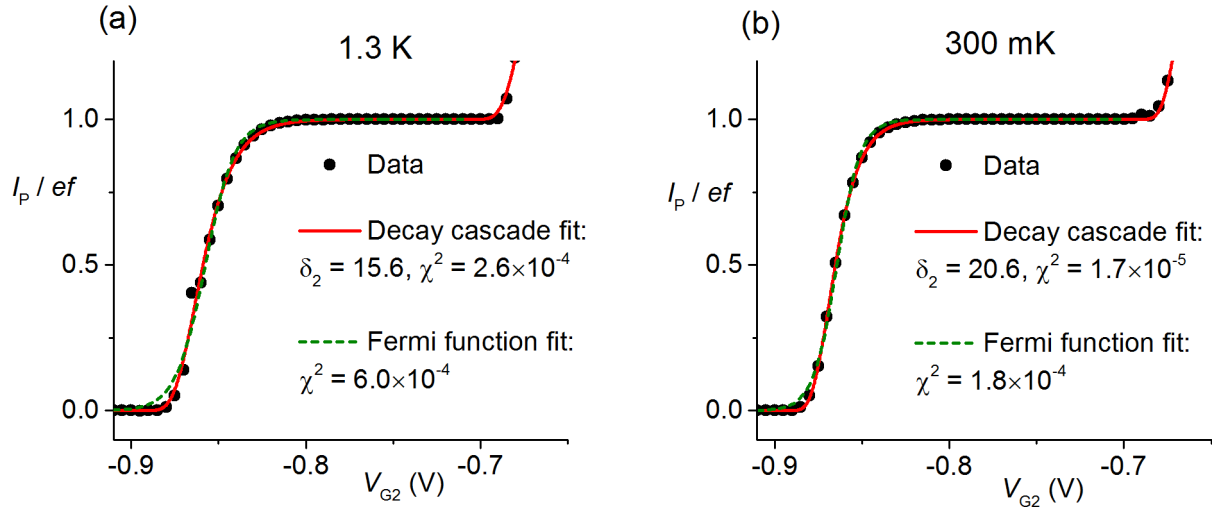


FIG. S3. Normalised pump current as a function of V_{G2} at temperatures of 1.3 K in panel (a), and 300 mK in panel (b). The gate voltages are tuned to the optimal working point used for the data of the main text, apart from $V_{G1} = -0.94$ V. Each data set has been fitted to the decay cascade model (equation (2) of the main text) and a Fermi function (equation (3) of the main text), with the independent variable V_{G3} in the equations replaced by V_{G2} . χ^2 values for the fits are indicated on the plot. As for the χ^2 values reported in the main text, χ^2 is the sum of the square of the fit residuals divided by the number degrees of freedom.